HHS Public Access

Author manuscript

Langmuir. Author manuscript; available in PMC 2022 November 28.

Published in final edited form as:

Langmuir. 2020 June 23; 36(24): 6626–6634. doi:10.1021/acs.langmuir.0c00320.

Lipid Shell Retention and Selective Binding Capability Following Repeated Transient Acoustic Microdroplet Vaporization

Jennifer N. Harmon,

Chloe A. Celingant-Copie,

Foad Kabinejadian,

Joseph L. Bull

Department of Biomedical Engineering, Tulane University, New Orleans, Louisiana 70118, United States

Abstract

Targeted therapy and molecular imaging using ultrasound have been widely explored using microbubble contrast agents, and more recently, activatable droplet contrast agents that vaporize when exposed to focused ultrasound have been explored. These droplets are coated with a stabilizing, functionalizable shell, typically comprised of fully saturated phospholipids. While the shedding of the lipid shell under ultrasound exposure is a well-studied phenomenon in microbubbles, it has not been fully explored in droplet-based contrast agents, particularly in those that undergo a reversible phase change and recondense following vaporization. Here, we investigate the retention of the lipid shell following repeated transient vaporization events. Two separate fluorescent markers were used to track individual lipid subpopulations: PEGylated lipids, to which targeting ligands are typically bound, and non-PEGylated lipids, which primarily contribute to droplet stability. Following confirmation of the homogeneous surface distribution of each subpopulation of shell lipids using confocal microscopy, high-speed optical imaging provided visual evidence of the ability to repeatedly induce vaporization and recondensation in micron-scale droplets using 5.208 MHz, 3.17 MPa focused ultrasound pulses transmitted from an imaging transducer. Flow cytometry analysis indicated that while PEGylated lipids were fully retained following repeated transient phase change events, 20% of the bulk lipids were shed. While this likely contributed to an observed significant reduction in the average droplet diameter, the selective binding capabilities of droplets functionalized with an RGD peptide, targeted to the integrin $\alpha_v\beta_3$, were not affected. These results indicate that repeated droplet activation may promote shifts in the droplet size distribution but will not influence the accuracy of targeting for therapy or molecular imaging.

Graphical Abstract

Corresponding Author Joseph L. Bull – Department of Biomedical Engineering, Tulane University, New Orleans, Louisiana 70118, United States; Phone: (504) 865-5843; jbull@tulane.edu.

The authors declare no competing financial interest.

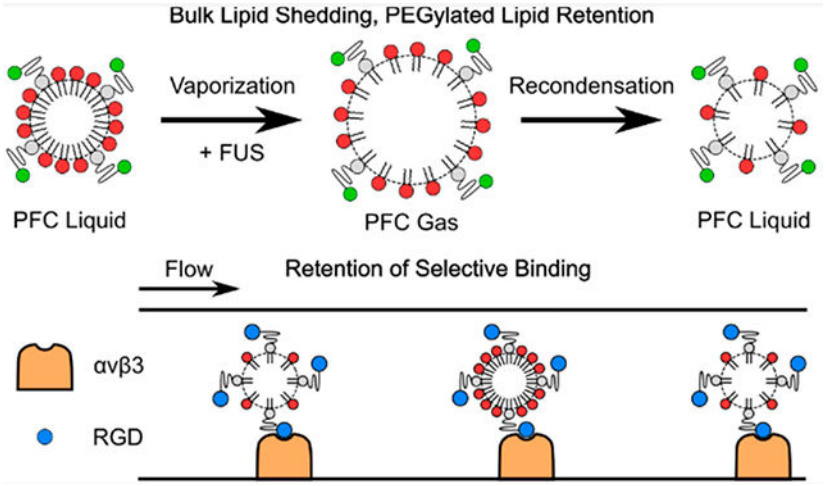

INTRODUCTION

Molecular imaging and targeted therapy using ultrasound have been widely investigated in recent years due to the widespread accessibility, cost-effectiveness, and safety of ultrasound.[1] These methods commonly utilize perfluorocarbon (PFC) microbubble contrast agents (MCAs) encapsulated with a surfactant shell that can be functionalized with a ligand targeted to a receptor of interest. MCAs will preferentially accumulate in regions expressing the targeted vascular marker. MCAs oscillate nonlinearly under ultrasound exposure, thereby enabling the isolation of received MCA signal from linear tissue signal, allowing for specific detection of the targeted MCAs in imaging applications.[2] Higher insonation pressures and duty cycles may be utilized in therapeutic applications, with the intention of releasing drugs from the surface of the MCAs or locally enhancing vascular permeability to enhance drug uptake.[3-5] These approaches have proven successful in the delivery of chemotherapeutics to tumors,[6] thrombolysis,[7] and more recently, in cancer immunotherapy.[8] Ultrasound molecular imaging has recently entered clinical trials,[1,9,10] and with the advent of molecular acoustic angiography techniques, spatial resolutions below 100 μm are rapidly becoming feasible.[11]

MCA-based approaches present a number of limitations, however. The relatively low circulation time of MCAs may reduce accumulation in receptor-expressing regions or limit the total possible imaging duration.[12,13] Additionally, in the context of drug delivery, MCAs are limited to loading drug into or onto the shell, limiting the amount of drug that can be loaded per bubble and resulting in variable encapsulation efficiencies.[14,15] Phase-change contrast agents (PCCAs) have been proposed as an alternative to ameliorate these issues.[16,17] PCCAs, which are comprised of a liquid perfluorocarbon (PFC) core and an encapsulating shell, vaporize when exposed to focused ultrasound (FUS) in a process termed acoustic droplet vaporization (ADV). The circulation time of these PCCAs is significantly higher than MCAs,[12] which allows for greater accumulation in target regions, and droplets are far better suited to drug loading than MCAs, achieving encapsulation efficiencies of up to 99% using a double emulsion geometry.[18,19] Additionally, the droplet composition and size can be tuned such that droplets either stably vaporize and remain microbubbles, with applications in gas embolotherapy,[20] or subsequently recondense (RC) back into droplets,

a phenomenon that has been widely explored in recent years for its applications in novel imaging methods, such as sono-photoacoustics.[21,22] The properties of the encapsulating shell of these agents are of great interest with respect to microbubble oscillation and destruction dynamics,[23] resistance to dissolution of the gaseous bubble core,[24] and targeting capabilities with respect to molecular imaging or local drug delivery, as ligands are typically covalently linked to poly(ethylene glycol) (PEG) chains protruding from the droplet or bubble surface.[9,25] Shells are most commonly comprised of fully saturated phospholipids due to their biocompatibility, ease of functionalization, and favorable dynamics for bubble oscillation.[26]

Shedding of the encapsulating lipid shell is a known phenomenon in microbubbles under continuous pulsed ultrasound exposure.[27-30] As these surfactants are shed from the shell, microbubbles become more prone to dissolution, reducing their circulation time, and the surface concentration of the targeting ligands is rapidly depleted, potentially leading to underestimates of receptor expression or to limited imaging durations with a single injection of microbubbles. The extensibility of this phenomenon to PCCAs has not been fully explored. While optical studies have qualitatively confirmed that some portion of the shell is retained following a single vaporization event[31] and that these bubbles retain their selective binding capabilities,[32] they do not investigate relative changes in the composition of the lipid shell. These previous studies have also primarily focused on stably vaporized droplets, rather than the investigation of droplets that undergo multiple ADV/RC events. Given that lipid shedding in microbubbles was observed to be dependent on oscillation amplitude[27,29,30] and that ADV/RC involves rapid, high amplitude changes in particle diameter (up to 5x diameter),[33] it is feasible that repeated ADV/RC events may drive substantial lipid shedding.

The primary purpose of the current study is to investigate changes in two relevant subpopulations of lipids present on the droplet shell: bulk lipids, primarily responsible for stability and resistance to droplet coalescence or dissolution or in-gassing while particles are in the bubble phase prior to RC, and PEGylated lipids, which are crucial for targeting. Droplet shells were labeled with DiI, a fluorescent marker previously used as an analog for the lipid shell in microbubble experiments[29,34] to track bulk lipids. PEGylated lipids were labeled with Alexa Fluor 488. Droplets were exposed to FUS to repeatedly induce ADV/RC. Following a set number of ADV/RC events, the relative surface concentration of each lipid subpopulation as compared to controls was evaluated using flow cytometry. It was determined that 20% of the bulk lipids were shed during ADV/RC, potentially contributing to an observed reduction in the average droplet diameter following ADV/RC by reducing resistance to bubble dissolution during the transient gaseous phase. However, the PEGylated lipids were fully retained. To confirm the retention of selective binding efficacy, benchtop binding assays were conducted. A cyclic RGD peptide was conjugated to the terminal amine group on the PEG chains to target the integrin $\alpha_v\beta_3$, a marker commonly overexpressed in highly vascular cancers.[35,36] No loss in selective binding efficacy was observed, as expected following the confirmation of full retention of the PEGylated lipids. These results indicate that while coalescence, ingassing, or dissolution during the gaseous phase of the ADV/RC event may be enhanced or accelerated after a large number of ADV/RC events, selective targeting to receptor expressing regions will not be impacted.

EXPERIMENTAL SECTION

Droplet Fabrication.

A lipid thin film was prepared by combining 1,2-distearoyl-*sn*-glycero-3-phosphocholine (DSPC, Avanti Polar Lipids, Alabaster, AL, USA) and either 1,2-distearoyl-*sn*-glycero-3-phosphoethanolamine-*N*-[amino(polyethylene glycol)-2000] (ammonium salt) (DSPE-PEG2000-Amine, Avanti Polar Lipids) or 1,2-distearoyl-*sn*-glycero-3-phosphoethanolamine-*N*-[maleimide(polyethylene glycol)-2000] (ammonium salt) (DSPE-PEG2000-Mal, Avanti Polar Lipids) dissolved in chloroform in a 90:10 mol % ratio. The lipids were dried under a vacuum and subsequently hydrated with a diluent comprised of phosphate buffered saline (PBS, 80% v/v, Thermo Fisher Scientific, Waltham, MA, USA), propylene glycol (10% v/v, Sigma-Aldrich, St. Louis, MO, USA), and glycerol (10% v/v, Sigma-Aldrich) and the mixture was heated to 70 °C for 15 min to produce a lipid blend. After cooling to room temperature, perfluorohexane (PFH, Strem Chemicals, Newburyport, MA, USA) was added to the lipid blend in a 1:3 volumetric ratio (PFH: lipid blend) prior to sonication for 15 s on ice (Q55, 55 W, 20 kHz, QSonica, Newtown, CT, USA). The resulting emulsion was washed thrice using repeated centrifugation. For each wash, the droplet suspension was centrifuged at 6000 rpm for 45–60 s using a minicentrifuge (Fisher Scientific, Hampton, NH, USA) until a pellet was formed; the supernatant was then removed and replaced with fresh lipid diluent. For further washing, the pellet was resuspended using gentle pipet aspiration prior to the next round of centrifugation. The initial volumetric droplets-to-diluent ratio was 1:5 (e.g., 100 μL unwashed droplet suspension to 500 μL lipid diluent).

Three separate droplet populations were used for this study: (1) Vybrant DiI (Molecular Probes, Eugene, OR, USA) labeled, for tracking DSPC, (2) Alexa Fluor 488 (AF488, Molecular Probes) labeled, for tracking DSPE-PEG2000, and (3) cyclo(Arg-Gly-Asp-Phe-Cys) (cRGDfC, Peptides International, Louisville, KY, USA) conjugated, for selective targeting to $\alpha_v\beta_3$. DiI and AF488 labeled droplets contained DSPE-PEG2000-Amine, whereas cRGDfC conjugated droplets contained DSPE-PEG2000-Mal. DiI labeling consisted of incubating droplets (5.5×10^8 per ml) with 20 μM DiI (1:10 v/v droplets to DiI) in the aforementioned lipid diluent at room temperature for 1 h. AF488 was covalently linked to the end of the PEG brush via a peptide bond. Droplets (5.5×10^8 per ml) were incubated with AF488 containing an amine reactive group (Alexa Fluor 488 sulfodichlorophenol ester, 5x molar ratio, A30052, Thermo Fisher Scientific) at room temperature for 1 h in a pH 8.3 sodium bicarbonate buffer. cRGDfC was covalently coupled to the terminal maleimide group on the PEG brush via a cysteine-maleimide linkage. Droplets (1.4×10^9 per ml) were incubated with cRGDfC (5x molar ratio) at room temperature overnight in a pH 6.5, 50 mM HEPES buffer (Sigma-Aldrich) containing 80% PBS, 10% propylene glycol, and 10% glycerol. For the binding assay, a nonselective cyclo(Arg-Ala-Asp-Phe-Cys) peptide (cRADfC, Peptides International) was substituted for cRGDfC as a negative control. All droplets were washed thrice following the labeling step. The orientation of each label with respect to the shell lipids is shown in Figure 1.

Droplet Sizing.

The size distribution of each droplet population was assessed using a Coulter Counter (Multisizer 4e, Beckman-Coulter, Brea, CA, USA). A representative population of cRGDfC conjugated droplets measured 1.508 ± 0.690 μm in diameter. For DiI and AF488 labeled populations, both control and experimental populations were sized following the ADV/RC experiments to determine if ADV/RC resulted in a shift in droplet size distribution. These data are addressed in the results and discussion. Representative initial size distributions measured 1.643 ± 0.950 μm and 1.707 ± 0.800 μm for the DiI and AF488-conjugated droplets, respectively. Statistical analysis was conducted using independent *t* tests between control and experimental groups using the SciPy stats package (v1.3.2).[37,38] One-sample *t* tests were used to evaluate the shift or lack thereof in droplet concentration following ADV/RC.

Acoustic Droplet Vaporization.

A custom ultrasound guided FUS method, described previously,[39] was used to target and induce ADV/RC in a manner relevant to image-guided therapy and molecular imaging applications. Briefly, a custom Matlab script (MathWorks Inc., Natick, MA, USA) specifying the interleaved imaging and FUS pulse sequence and GUI controls was written for operation with a Verasonics Vantage 256 Research Ultrasound system (Verasonics Inc., Kirkland, WA, USA) and a 5.208 MHz linear array transducer (L7–4, Philips, Amsterdam, Netherlands). This method allows for fine software control over the placement of the focal spot in the *X*–*Z* plane, as well as the definition of multiple focal spots to insonate. The FUS beam profile geometry is shown in Figure 2A-C. FUS was operated at 3.17 MPa peak negative pressure (PNP), 25 voltage cycles, and an effective 3500 Hz pulse repetition frequency. The mechanical index (1.39) was selected to remain within FDA safety limits (≤1.9 MI) while still exceeding the PNP threshold required to induce ADV. The observed ADV threshold (i.e., minimal acoustic parameters at which consistent ADV was observed) in this experimental setup was 10 voltage cycles, 2.21 MPa PNP; this was determined optically during the high-speed imaging experiments. The occurrence of ADV was defined as a visually observable diameter fluctuation during the droplet to bubble conversion phase.

For flow cytometry and binding assay experiments, droplets were placed into wells in a custom polydimethylsiloxane (PDMS) construct (10 μL total volume per well, 3 × 10^6 droplets per well) for FUS exposure. The PDMS well construct, suspended above a scattering and attenuating surface-roughened PDMS block to minimize acoustic reflections, was sealed with an acoustically transparent membrane (Tegaderm, 3M, Maplewood, MN, USA) and placed into an acrylic tank containing degassed water maintained at 37 °C. Wells containing droplets were located using B-mode ultrasound imaging. Masks were then drawn over the target well using GUI controls to generate a 5 × 1 matrix of focal spots within the well, spaced 460 μm laterally, ensuring the full well was exposed to the full width at half-maximum (fwhm) of the FUS pulses. Each focal spot was exposed to 250 FUS pulses in total (1250 pulses per well). Following ADV/RC, the membrane was removed from the PDMS construct, and droplet suspensions were collected for further analysis. The PDMS constructs, insonation setup, and FUS guidance are pictured in Figure 2D-F.

High Speed Optical Imaging.

A Phantom high-speed camera (VEO710, FAST option, Vision Research, Wayne, NJ, USA) operated at 580000 frames per second was used to optically image ADV/RC. Droplets were placed on the bottom of an acrylic tank filled with degassed water maintained at 37 °C and placed over an inverted microscope (Eclipse Ti2, Nikon). The ultrasound transducer was aligned such that the focal spot was centered in the viewing frame. The transducer was angled to prevent acoustic reflections from interfering with droplet behavior. Droplets were exposed to FUS while capturing video at 128 × 32 pixel resolution. Videos were then stepped through frame by frame to identify repeated ADV/RC in single droplets. Images were cropped to isolate single droplets/bubbles and contrast was enhanced using ImageJ (0.3% saturated pixels, National Institutes of Health, Bethesda, MD, USA) to highlight droplet/bubble boundaries. All images were processed in the same manner for display.

Confocal Microscopy.

Images of AF488 and DiI labeled droplets were captured using an inverted point scanning confocal microscope (Ti2 Eclipse, Nikon) equipped with a 60x oil immersion objective (Nikon). Images were processed using NIS Elements software (Nikon). AF488 and DiI labeled droplets were imaged using 488 nm λ_{ex}, 535/45 nm λ_{em} (FITC) and 531 nm λ_{ex}, 595/50 nm λ_{em} (TRITC), respectively. Images were captured either at 60x or at 1200x using optical zoom.

Flow Cytometry.

An acoustic focusing flow cytometer (Attune Acoustic Focusing Cytometer, Applied Biosystems, Foster City, CA, USA) was used to confirm successful droplet shell labeling as compared to unlabeled controls and to quantitatively assess the relative surface concentration of shell lipids following ADV/RC. A 488 nm excitation laser was used for both AF488 and DiI labeled droplets coupled with 530/30 nm (BL1) and 574/26 nm (BL2) emission filters, respectively. The positive/negative fluorescence signal threshold for gating was selected based on the results from unstained samples. Median fluorescence signal values, calculated from analyzed droplets above the positive/negative threshold, were used to quantify each sample. The same settings for the gain on the detectors were used across experimental and control samples. Each independent sample consisted of 150000 analyzed droplets above the positive fluorescence signal threshold. Data are displayed using histograms with a linearly scaled *x*-axis. Data were collected using Attune cytometric software packaged with the flow cytometer (v2.1.0, Applied Biosystems) and quantified and analyzed using FlowCytometryTools (v0.5.0), a Python package. Plots were generated using Matplotlib (v3.1.1).[40] Statistical analysis was conducted using independent *t* tests between control and experimental groups using the SciPy stats package (v1.3.2).[37,38]

Parallel Plate Flow Chamber Binding Assay.

Binding assays were conducted to determine if droplets retained selective binding capabilities after ADV/RC. The integrin $\alpha_v\beta_3$ (3050-AV-050, R&D Systems, Minneapolis, MN, USA), purchased in powder form, was reconstituted in PBS at 25 μg/mL; 5 μL of the integrin solution was pipetted onto a glass slide and allowed to adsorb overnight

in the fridge. The following day, the slide was gently washed with PBS and blocked for 1 h at room temperature using a 10 mg/mL bovine serum albumin (BSA, BP1600, Fisher Scientific, Hampton, NH, USA) solution to prevent nonspecific binding. The slide was washed once more with PBS before mounting into a parallel plate flow chamber (GlycoTech, Gaithersburg, MD, USA). The flow chamber was then placed onto an inverted microscope (Eclipse Ti2, Nikon, Tokyo, Japan) and connected to a syringe pump (Fisher Scientific). A flow rate of 1 mL/min was used for each step. Experiments were conducted at room temperature (25 °C). The chamber was primed with 1 mL of PBS prior to running 5 mL of a 1:2000 v/v dilution of droplet suspension to PBS. The slide was then washed with 5 mL of PBS. Images were captured using a camera mounted to the microscope (Blackfly S, FLIR Systems, Wilsonville, OR, USA) at 40× magnification; 5 images each were captured inside and outside of the receptor-adsorbed region. Images were processed using a custom Matlab script to count droplets. A selective binding ratio (droplets in receptor region/droplets outside of receptor region) was calculated for each sample. A cRADfC control was run as a negative control to ensure results were not influenced by nonselective binding. Statistical analysis was conducted using paired *t* tests between receptor adsorbed and nonreceptor adsorbed regions within groups, and independent *t* tests to compare binding ratios between groups, using the SciPy stats package (v1.3.2).[37,38]

RESULTS AND DISCUSSION

Fluorophore Coating of Droplet Shells.

The fluorophore distribution across the droplet shell was investigated using confocal microscopy. Previous studies have observed clustering of PEGylated lipid subpopulations on the surface of microbubbles with similar lipid compositions to the droplet shells used in this study.[41] This phenomenon may influence lipid shedding. It has been hypothesized that supersaturation of lipids and associated shell buckling in localized regions of the shell are implicated in the expulsion of lipids during bubble dissolution;[42] it is therefore reasonable to hypothesize that augmented local concentrations of PEGylated lipids may lead to increased steric interference and shell buckling, and therefore lipid shedding, during the compressive phase of bubble oscillation or RC in the context of this study. Fluorescent images of the droplets used for the present study, however, indicated that both DiI and AF488 evenly coated the droplet shells (Figure 3), corresponding to even coatings of DSPC and DSPE-PEG2000, respectively. The results, therefore, were not influenced by the distribution of lipid subpopulations on the shell.

Optical Imaging of ADV/RC.

Imaging and therapeutic applications that are reliant on ADV/RC typically utilize nanoscale droplets (<200 nm) due to the influence of droplet diameter on RC capabilities and the ability to image the extravascular space.[22,43] However, while flow cytometry is commonly used to detect cell uptake of nanoparticles,[44,45] particles in this size range are prone to a number of measurement errors with conventional flow cytometers when measured freely in suspension, including severely reduced signal-to-noise ratios and increased coincidence counting artifacts, rendering it difficult to determine the accuracy of the results.[46,47] The use

of micron-scale droplets therefore facilitated accurate analysis of shell retention using flow cytometry.

To confirm the occurrence of the ADV/RC phenomenon with the micron-scale PFH droplets used for this study, high speed optical imaging experiments were conducted. Cine loops with 4 s durations were captured at 580000 frames per second. High frame rate videos were captured immediately following FUS pulses to elucidate droplet behavior. Repeated ADV/RC in single droplets was consistently observed. Given that an insonation frequency of 5.208 MHz was utilized and the video sampling frequency was near an order of magnitude lower, it is probable that these events were under-sampled, and the full extent of the diameter fluctuation over the course of the phase change, as well as the true time scale for a single ADV/RC event, cannot be determined from these data. However, the consistent reversibility of the phase change event irrespective of the number of times a given droplet has already undergone ADV/RC can be confirmed. Assuming that droplets at minimum underwent ADV/RC once per FUS pulse, and at maximum underwent ADV/RC once every cycle, every FUS pulse—vaporizing during the peak negative and recondensing during the peak positive—then single droplets were observed undergoing ADV/RC between 93 times at minimum and 2325 times at maximum before being pushed out of the viewing frame by acoustic radiation force. These data indicate that repeated, reversible vaporization events can be induced in the micron-scale droplets used for this study, confirming the ability to investigate lipid shedding using these agents. The repeatedly reversible nature of the phase change is in agreement with experiments performed in nanoscale droplets.[22,43] While the true diameter fluctuation amplitude and time scale for a single ADV/RC event in micron-scale droplets will be investigated in future work using higher frame rate imaging, with a particular emphasis on determining the degree and duration of the bubble expansion phase after nucleation and prior to recondensation, these data are not necessary for interpretation of the current results or validation of the experimental systems used. Figure 4 illustrates an ADV/RC event captured using high speed imaging.

Retention of Shell Lipids Following ADV/RC.

Fluorescently labeled droplets were exposed to a total of 250 FUS pulses—3.17 MPa, 5.208 MHz, 25 cycles per pulse—to repeatedly induce ADV/RC to determine if numerous reversible phase change events promote shedding of the lipid shell. Droplet samples that had either been exposed to FUS or treated identically without the FUS exposure were analyzed using a flow cytometer. The median fluorescence intensity in the positively staining population was measured as an analog to the surface concentration of the fluorophore of interest and, by extension, the relative concentration of the lipid subpopulation tracked by that fluorophore. DSPC, the bulk lipid (90 mol %) on the droplet shell, was tracked using DiI, whereas PEGylated lipids (10 mol %) were tracked using AF488. It should be noted that droplets were labeled either with DiI or with AF488 and not with both simultaneously, due to considerable spectral overlap when using the excitation/emission combinations available to us on our flow cytometer. These droplet populations were used independently in separate experiments and were analyzed independently.

Representative examples of the lack of a shift in AF488 intensity, and the observed shift in DiI intensity following ADV/RC as compared to a control are shown in Figure 5A,B. Figure 5C displays the results averaged by group for each set of droplets. It was determined that while AF488 fluorescence was not affected by ADV/RC ($N = 5$, $p > 0.05$), the average DiI median fluorescence was reduced by 20% ($N = 5$, $p < 0.05$). This indicated that while PEGylated lipids were retained on the shell, DiI and the associated bulk lipids were shed.

Although preferential DiI ejection from the membrane while the lipids themselves remain intact in the shell would explain the decrease in fluorescence intensity observed in the bulk lipid case, it is not a possible confounding factor for these results. DiI is only strongly fluorescent when embedded in a lipid membrane; fluorescence will not be detected if it is ejected from the shell into the surrounding aqueous medium.[48] It has been shown that DiI exposed to lipid membranes will rapidly diffuse throughout the membrane; any DiI independently expelled from the shell would have rapidly reentered the membrane and no overall change in fluorescent signal would have been observed.[49] Additionally, DiI has previously been demonstrated to serve as an effective analog for the dynamics of the lipids within the shell of ultrasound contrast agents,[29] further indicating that DiI behavior is an effective analog for lipid behavior. However, to address potential concerns about the use of DiI as a direct marker of lipid behavior, future studies will compare the behavior of DiI-labeled droplets to those fabricated with bulk lipids bearing a covalently attached fluorophore.

Here, we hypothesize that the fluorescence decrease can be explained by the formation and subsequent transport of DiI labeled lipid micelles or liposomes formed upon ejection of lipids from the droplet shell. Previous studies investigating lipid shedding from microbubbles determined that micelle formation occurred above a bubble oscillation amplitude threshold of 1.3-fold;[29] the maximal possible diameter fluctuation amplitude for the ADV/RC event is 5-fold[33] based on the diameter change from a single stable ADV event. The minimal possible diameter fluctuation, determined from our likely under-sampled high-speed optical investigation of ADV/RC, was 1.87-fold (Figure 4), well above the reported oscillation amplitude threshold for lipid shedding and micelle formation from microbubbles. Lipid micelle formation and transport from the bubble surface was observed as the primary method of lipid shedding in the aforementioned microbubble study.[29] It is reasonable to conclude that similar mechanisms would govern lipid shedding during ADV/RC, indicating that the primary mechanism of shell loss was via the generation of DiI labeled lipid micelles. These nanoscale lipid micelles (100s of nm)[29] will fall below the effective detection limit of the flow cytometer, thereby minimizing any potential impact on the observed results.[46,47]

Future experiments should utilize high-speed imaging under fluorescence illumination to confirm the mechanism of lipid shedding during ADV/RC, with a particular emphasis on elucidating the physical underpinnings of the disparity in lipid expulsion between the two different species. An appropriately sampled optical evaluation of the full ADV/RC process will indicate at which point lipids are shed (e.g., at maximal bubble diameter following expansion, or a later time point during the RC phase), a critical piece of information for understanding the mechanism. This will also serve as an effective test for DiI-labeled micelle expulsion from the lipid shell, as the bulk lipid shedding mechanism may vary

between ADV/RC and microbubble oscillation. Additionally, this optical method may provide better sensitivity than the methods used in the current study; the sensitivity of current methods may be masking the expulsion of some PEGylated lipids.

Droplet Size Distributions Following ADV/RC.

The flow cytometry results indicated that bulk lipids were shed following repeated ADV/RC events; this may result in droplets that are more prone to coalescence as the surface concentration of stabilizing shell lipids has been reduced, and depending on the time scale of the ADV/RC events, droplets that are more prone to shifts in size distributions due to diffusion of the transiently gaseous core into the surrounding medium or due to ingassing. The size distributions of droplets exposed to ADV/RC and control groups were assessed using a Coulter Counter. A decrease of 0.217 and 0.337 μm in average droplet diameter was observed in the AF488-labeled and DiI-labeled groups, respectively. These shifts were significant as compared to controls for both groups ($N = 5$ each, $p < 0.05$), indicating that while bulk lipid presence was tracked only in the DiI group, the effects of bulk lipid shedding were observed in all droplets exposed to ADV/RC. Given that the medium in which ADV/RC was conducted had been degassed, these results are likely explained by the diffusion of PFC into the surrounding medium during the transient gaseous phase. However, *in vivo*, this result may be reversed due to ingassing dominating over PFC dissolution.

It should be noted that the droplet concentration was not significantly different for either the AF488 or DiI group as compared to the initial concentration loaded into the well ($N = 5$, $p > 0.05$), indicating that the shift in the droplet size distribution cannot be explained by the selective depletion of larger droplets coalescing during the transient gaseous phase and stably vaporizing rather than recondensing. Additionally, the shift in size distribution was not responsible for the results observed with flow cytometry; while both droplet populations exhibited a significantly reduced average diameter following ADV/RC, no change in AF488 median fluorescence intensity as compared to controls was observed. The variation in fluorescence values therefore cannot be explained by the variation in average droplet diameter.

Selective Binding of Droplets Following ADV/RC.

The selective binding capabilities of the droplets following ADV/RC were examined using benchtop binding assays. Droplets bearing either a cRGDfC peptide, targeted to the integrin $\alpha_v\beta_3$, or a cRADfC peptide, a nontargeted negative control, were run through a parallel plate flow chamber bound to a glass slide with a small region containing adsorbed $\alpha_v\beta_3$. A selective binding ratio, as determined by the number of droplets bound within the $\alpha_v\beta_3$ coated region divided by the number of droplets bound outside of the $\alpha_v\beta_3$ coated region, was assessed for negative control droplets as well as for positive control droplets (no FUS) and droplets that had undergone ADV/RC. The results are illustrated in Figure 6.

The lack of selective binding with cRADfC droplets confirmed that results were due to specific receptor–ligand interactions between cRGDfC and $\alpha_v\beta_3$. It was determined that both control and ADV/RC droplet populations had significantly higher selective binding ratios than the negative control (non-normalized: 3.39 ± 0.983 and 2.99 ± 0.707,

respectively, compared to 0.660 ± 0.140, mean ± SEM, $N = 5$ each, $p < 0.05$), indicating that ADV/RC did not result in the loss of selective binding capabilities. The binding ratio did not vary significantly between the control and ADV/RC groups ($N = 5$, $p > 0.05$). These results agree with the flow cytometry data; given that the PEGylated lipids were determined to be fully retained following ADV/RC and the targeting ligands are conjugated to the terminal maleimide on the PEG chain, these results are consistent. These results indicate that repeated ADV/RC conducted at the acoustic parameters used in this work will not reduce the ability of droplets to bind to selected molecular targets, ensuring adequate targeting for therapeutic and diagnostic applications. It should be noted, however, that while selective targeting is maintained following ADV/RC, the shift in the droplet size distribution may still result in an underestimate of relative receptor expression levels in the context of molecular imaging. A smaller average droplet diameter corresponds to a higher ADV threshold; assuming constant acoustic parameters are used through an imaging session, the vaporization efficiency (i.e., the fraction of available droplets vaporized per pulse within a given volume) will progressively decrease, resulting in lower amplitude received signals at later time points despite a similar droplet concentration within a region of interest.

One additional caveat to be considered is that while this particular assay confirmed the functional retention of the PEGylated lipids, there may be some shedding below the detection threshold of the methods used in the current study. While this did not result in a functional difference in the selective binding efficacy when using the acoustic parameters reported here, a higher acoustic pressure (i.e., potentially higher amplitude diameter fluctuation), pulse width, or pulse repetition frequency (i.e., increased number of ADV/RC events) may drive further lipid shedding, potentially resulting in a loss of binding functionality if PEGylated lipids are indeed being shed below the current detection limits. Future studies will utilize more sensitive methods, either the aforementioned optical method, with ultrahigh speed imaging under fluorescence illumination or direct spectroscopic analysis of the droplet shell (e.g., with NMR spectroscopy), to assess the retention of PEGylated lipids. Varying acoustic parameters will also be tested to determine if lipid shedding is purely a threshold based phenomenon or if the magnitude of lipid shedding is “dose-dependent”.

SUMMARY AND CONCLUSIONS

This study has determined that repeated ADV/RC in PFH microdroplets drove the shedding of bulk phospholipids from the droplet shell while PEGylated lipids were fully retained. These changes in the lipid composition of the droplet shell promoted shifts in the droplet size distribution after repeated ADV/RC but did not influence the selective binding capabilities of the droplets. These results indicate that repeated droplet activation via ADV/RC will not hamper the efficacy of targeted therapies but may influence estimates of relative receptor expression during quantitative molecular imaging sessions due to the shifting droplet size distribution.

ACKNOWLEDGMENTS

This work was supported by NIH grant R01EB006476. J.S.H. is supported by a Louisiana Board of Regents Support Fund Fellowship.

REFERENCES

(1). Abou-Elkacem L; Bachawal SV; Willmann JK Ultrasound molecular imaging: Moving toward clinical translation. Eur. J. Radiol 2015, 84 (9), 1685–93. [PubMed: 25851932]

(2). deJong N; Bouakaz A; Frinking P Harmonic imaging for ultrasound contrast agents. 2000 IEEE Ultrasonics Symposium. Proceedings. An International Symposium (Catal. No.00CH37121) 2000, 2, 1869–1876.

(3). Guvener N; Appold L; de Lorenzi F; Golombek SK; Rizzo LY; Lammers T; Kiessling F Recent advances in ultrasound-based diagnosis and therapy with micro- and nanometer-sized formulations. Methods 2017, 130, 4–13. [PubMed: 28552267]

(4). Lentacker I; De Smedt SC; Sanders NN Drug loaded microbubble design for ultrasound triggered delivery. Soft Matter 2009, 5 (11), 2161.

(5). Theek B; Baues M; Ojha T; Mockel D; Veettil SK; Steitz J; van Bloois L; Storm G; Kiessling F; Lammers T Sonoporation enhances liposome accumulation and penetration in tumors with low EPR. J. Controlled Release 2016, 231, 77–85.

(6). Abdalkader R; Kawakami S; Unga J; Suzuki R; Maruyama K; Yamashita F; Hashida M Evaluation of the potential of doxorubicin loaded microbubbles as a theranostic modality using a murine tumor model. Acta Biomater. 2015, 19, 112–8. [PubMed: 25795624]

(7). Wang X; Gkanatsas Y; Palasubramaniam J; Hohmann JD; Chen YC; Lim B; Hagemeyer CE; Peter K Thrombus-Targeted Theranostic Microbubbles: A New Technology towards Concurrent Rapid Ultrasound Diagnosis and Bleeding-free Fibrinolytic Treatment of Thrombosis. Theranostics 2016, 6 (5), 726–38. [PubMed: 27022419]

(8). Tu J; Zhang H; Yu J; Liufu C; Chen Z Ultrasound-mediated microbubble destruction: a new method in cancer immunotherapy. OncoTargets Ther. 2018, 11, 5763–5775.

(9). Wang S; Hossack JA; Klibanov AL Targeting of microbubbles: contrast agents for ultrasound molecular imaging. J. Drug Target 2018, 26, 420–434. [PubMed: 29258335]

(10). Wischhusen J; Padilla F Ultrasound Molecular Imaging with Targeted Microbubbles for Cancer Diagnostics: From Bench to Bedside. Irbm 2019, 40 (1), 3–9.

(11). Lindsey BD; Shelton SE; Foster FS; Dayton PA Assessment of Molecular Acoustic Angiography for Combined Microvascular and Molecular Imaging in Preclinical Tumor Models. Mol. Imaging Biol 2017, 19 (2), 194–202. [PubMed: 27519522]

(12). Rojas JD; Dayton PA Optimizing Acoustic Activation of Phase Change Contrast Agents with the Activation Pressure Matching Method: A Review. IEEE Trans Ultrason Ferroelectr Freq Control 2017, 64 (1), 264–272. [PubMed: 27740481]

(13). Ferrara K; Pollard R; Borden M Ultrasound microbubble contrast agents: fundamentals and application to gene and drug delivery. Annu. Rev. Biomed. Eng 2007, 9, 415–47. [PubMed: 17651012]

(14). Mullick Chowdhury S; Lee T; Willmann JK Ultrasound-guided drug delivery in cancer. Ultrasonography 2017, 36 (3), 171–184. [PubMed: 28607323]

(15). Wang TY; Wilson KE; Machtaler S; Willmann JK Ultrasound and Microbubble Guided Drug Delivery: Mechanistic Understanding and Clinical Implications. Curr. Pharm. Biotechnol 2014, 14 (8), 743–752.

(16). Kripfgans OD; Fowlkes JB; Miller DL; Eldevik OP; Carson PL Acoustic droplet vaporization for therapeutic and diagnostic applications. Ultrasound Med. Biol 2000, 26 (7), 1177–89. [PubMed: 11053753]

(17). Sheeran PS; Dayton PA Phase-Change Contrast Agents for Imaging and Therapy. Curr. Pharm. Des 2012, 18 (15), 2152–2165. [PubMed: 22352770]

(18). Fabiilli ML; Lee JA; Kripfgans OD; Carson PL; Fowlkes JB Delivery of water-soluble drugs using acoustically triggered perfluorocarbon double emulsions. Pharm. Res 2010, 27 (12), 2753–65. [PubMed: 20872050]

(19). Moncion A; Lin M; O'Neill EG; Franceschi RT; Kripfgans OD; Putnam AJ; Fabiilli ML Controlled release of basic fibroblast growth factor for angiogenesis using acoustically-responsive scaffolds. Biomaterials 2017, 140, 26–36. [PubMed: 28624705]

(20). Harmon JS; Kabinejadian F; Seda R; Fabiilli ML; Kuruvilla S; Kuo CC; Greve JM; Fowlkes JB; Bull JL Minimally invasive gas embolization using acoustic droplet vaporization in a rodent model of hepatocellular carcinoma. Sci. Rep 2019, 9 (1), 11040. [PubMed: 31363130]

(21). Li DS; Schneewind S; Bruce M; Khaing Z; O'Donnell M; Pozzo L Spontaneous Nucleation of Stable Perfluorocarbon Emulsions for Ultrasound Contrast Agents. Nano Lett. 2019, 19 (1), 173–181. [PubMed: 30543289]

(22). Li DS; Yoon SJ; Pelivanov I; Frenz M; O'Donnell M; Pozzo LD Polypyrrole-Coated Perfluorocarbon Nanoemulsions as a Sono-Photoacoustic Contrast Agent. Nano Lett. 2017, 17 (10), 6184–6194. [PubMed: 28926276]

(23). Borden MA; Kruse DE; Caskey CF; Zhao S; Dayton PA; Ferrara K Influence of Lipid Shell Physicochemical Properties on Ultrasound-Induced Microbubble Destruction. IEEE Trans Ultrason Ferroelectr Freq Control 2005, 52 (11), 1992–2002. [PubMed: 16422411]

(24). Sarkar K; Katiyar A; Jain P Growth and dissolution of an encapsulated contrast microbubble: effects of encapsulation permeability. Ultrasound Med. Biol 2009, 35 (8), 1385–96. [PubMed: 19616160]

(25). Yeh JS; Sennoga CA; McConnell E; Eckersley R; Tang MX; Nourshargh S; Seddon JM; Haskard DO; Nihoyannopoulos P A Targeting Microbubble for Ultrasound Molecular Imaging. PLoS One 2015, 10 (7), No. e0129681. [PubMed: 26161541]

(26). Sirsi S; Borden M Microbubble Compositions, Properties and Biomedical Applications. Bubble Sci., Eng., Technol 2009, 1 (1–2), 3–17. [PubMed: 20574549]

(27). Cox DJ; Thomas JL Rapid shrinkage of lipid-coated bubbles in pulsed ultrasound. Ultrasound Med. Biol 2013, 39 (3), 466–74. [PubMed: 23245826]

(28). Kwan JJ; Borden MA Lipid monolayer collapse and microbubble stability. Adv. Colloid Interface Sci 2012, 183–184, 82–99.

(29). Luan Y; Lajoinie G; Gelderblom E; Skachkov I; van der Steen AF; Vos HJ; Versluis M; De Jong N Lipid shedding from single oscillating microbubbles. Ultrasound Med. Biol 2014, 40 (8), 1834–46. [PubMed: 24798388]

(30). O'Brien JP; Ovenden N; Stride E Accounting for the stability of microbubbles to multi-pulse excitation using a lipid-shedding model. J. Acoust. Soc. Am 2011, 130 (4), EL180–5. [PubMed: 21974489]

(31). Reznik N; Seo M; Williams R; Bolewska-Pedyczak E; Lee M; Matsuura N; Gariepy J; Foster FS; Burns PN Optical studies of vaporization and stability of fluorescently labelled perfluorocarbon droplets. Phys. Med. Biol 2012, 57 (21), 7205–17. [PubMed: 23060210]

(32). Matsunaga TO; Sheeran PS; Luois S; Streeter JE; Mullin LB; Banerjee B; Dayton PA Phase-change nanoparticles using highly volatile perfluorocarbons: toward a platform for extravascular ultrasound imaging. Theranostics 2012, 2 (12), 1185–98. [PubMed: 23382775]

(33). Kripfgans OD; Fowlkes JB; Woydt M; Eldevik OP; Carson PL In Vivo Droplet Vaporization for Occlusion Therapy and Phase Aberration Correction. IEEE Trans Ultrason Ferroelectr Freq Control 2002, 49 (6), 726–738. [PubMed: 12075966]

(34). Lajoinie G; Luan Y; Gelderblom E; Dollet B; Mastik F; Dewitte H; Lentacker I; de Jong N; Versluis M Non-spherical oscillations drive the ultrasound-mediated release from targeted microbubbles. Communications Physics 2018, 1 (1), 209 DOI: 10.1038/s42005-018-0020-9.

(35). Anderson CR; Hu X; Zhang H; Tlaxca J; Decleves AE; Houghtaling R; Sharma K; Lawrence M; Ferrara KW; Rychak JJ Ultrasound molecular imaging of tumor angiogenesis with an integrin targeted microbubble contrast agent. Invest. Radiol 2011, 46 (4), 215–24. [PubMed: 21343825]

(36). Li J; Zhou P; Li L; Zhang Y; Shao Y; Tang L; Tian S Effects of Cationic Microbubble Carrying CD/TK Double Suicide Gene and alphaVbeta3 Integrin Antibody in Human Hepatocellular Carcinoma HepG2 Cells. PLoS One 2016, 11 (7), No. e0158592. [PubMed: 27391603]

(37). Oliphant TE Python for Scientific Computing. Comput. Sci. Eng 2007, 9, 10–20.

(38). Millman KJ; Aivazis M Python for Scientists and Engineers. Comput. Sci. Eng 2011, 13, 9–12.

(39). Harmon JS; Kabinejadian F; Bull JL Ultrasound-Guided Gas Embolization Using a Single Linear Array Transducer. IEEE Int. Ultrason Symp 2019, 1193–1196.

(40). Hunter JD Matplotlib: A 2D Graphics Environment. Comput. Sci. Eng 2007, 9, 90–95.

(41). Borden M; Martinez GV; Ricker J; Tsvetkova N; Longo M; Gillies RJ; Dayton PA; Ferrara K Lateral Phase Separation in Lipid-Coated Microbubbles. Langmuir 2006, 22, 4291–4297. [PubMed: 16618177]

(42). Borden MA; Longo ML Dissolution Behavior of Lipid Monolayer-Coated, Air-Filled Microbubbles: Effect of Lipid Hydrophobic Chain Length. Langmuir 2002, 18, 9225–9233.

(43). Luke GP; Hannah AS; Emelianov SY Super-Resolution Ultrasound Imaging in Vivo with Transient Laser-Activated Nanodroplets. Nano Lett. 2016, 16 (4), 2556–9. [PubMed: 27035761]

(44). Salvati A; Nelissen I; Haase A; Åberg C; Moya S; Jacobs A; Alnasser F; Bewersdorff T; Deville S; Luch A; Dawson KA Quantitative measurement of nanoparticle uptake by flow cytometry illustrated by an interlaboratory comparison of the uptake of labelled polystyrene nanoparticles. Nano Impact 2018, 9, 42–50.

(45). Zucker RM; Daniel KM; Massaro EJ; Karafas SJ; Degn LL; Boyes WK Detection of Silver Nanoparticles in Cells by Flow Cytometry Using Light Scatter and Far-Red Fluorescence. Cytometry, Part A 2013, 83 (10), 962–972.

(46). Fattaccioli J; Baudry J; Ùmerard J-D; Bertrand E; Goubault C; Henry N; Bibette J Size and fluorescence measurements of individual droplets by flow cytometry. Soft Matter 2009, 5 (11), 2232.

(47). Zucker RM; Ortenzio JN; Boyes WK Characterization, detection, and counting of metal nanoparticles using flow cytometry. Cytometry, Part A 2016, 89 (2), 169–183.

(48). Invitrogen, Molecular Probes Handbook, A Guide to Fluorescent Probes and Labeling Technologies. 11th ed.; Life Technologies Corporation: Carlsbad, CA, 2010.

(49). Li Y; Song Y; Zhao L; Gaidosh G; Laties AM; Wen R Direct labeling and visualization of blood vessels with lipophilic carbocyanine dye DiI. Nat. Protoc 2008, 3 (11), 1703–8. [PubMed: 18846097]

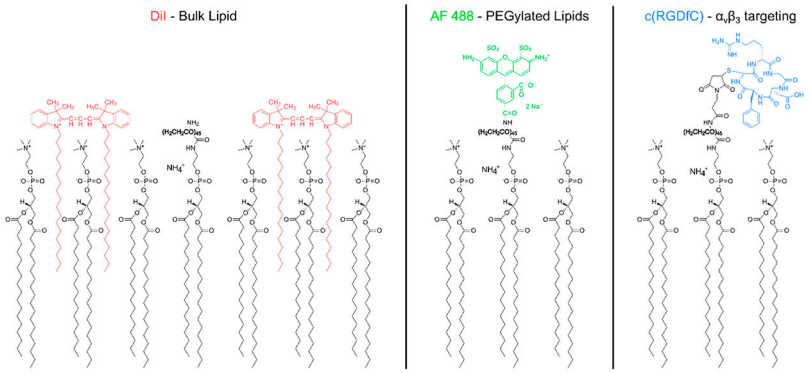

Figure 1.

Fluorophores and targeting peptides in relation to the lipid droplet shell. DiI (left) was used as a marker for DSPC, the primary or “bulk” lipid present on the droplet shell. Alexa Fluor (AF) 488 (center) was used as a marker for PEGylated lipids. For the binding assay experiments, a cyclic RGD peptide (right) was covalently linked to the terminal maleimide of the PEGylated lipids. The orientation of the markers and targeting peptide with respect to the lipid shell is shown. The 2000 molecular weight PEG chain is bolded. The shell composition is not to scale; the true ratio of DSPC to PEGylated lipids was 90:10 mol % for all droplets.

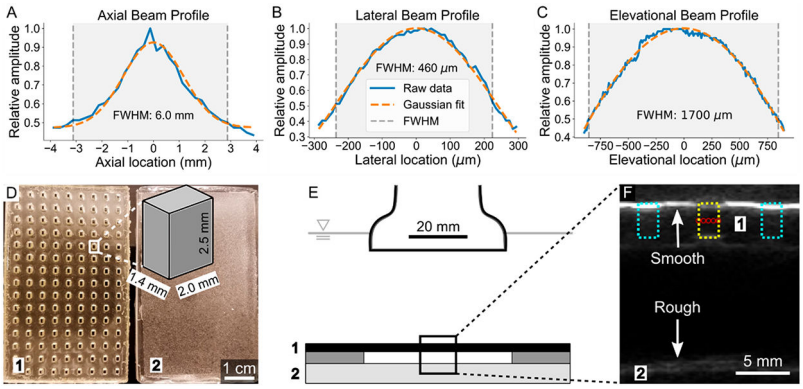

Figure 2.

Characterization of focused acoustic beam and depiction of experimental setup. (A–C) The profile of the FUS beam in the axial, lateral, and elevational axes is displayed. The relative amplitude is plotted against location, centered at the maximal amplitude location of the beam. The full width at half-maximum (fwhm), calculated using the raw data rather than the Gaussian fits, is shaded. (D) A top down view of the PDMS well construct used to hold the droplets (1) is shown alongside the PDMS scatterer/absorber used to prevent acoustic reflections from influencing droplet behavior (2). The dimensions of a single well are shown in the zoomed schematic; the full well is within the fwhm of the FUS beam when using 5 focal spots evenly spaced in the lateral axis. (E) A schematic of the ADV setup is shown. ADV/RC experiments were conducted in an acrylic tank filled with degassed water maintained at 37 °C. The PDMS well construct (1) was loaded with droplets, covered on both sides with an acoustically transparent membrane, and placed above the PDMS scatterer/absorber (2) using two additional PDMS spacers. This setup minimized the possibility of acoustic reflections interacting with droplets. (F) B-mode ultrasound was used to guide FUS pulses to the droplet containing wells. One such well is outlined in yellow (center) and the 5 evenly spaced (460 μm separation) focal spots for insonation are indicated with red circles. The adjacent wells (cyan) are filled with air and are easily distinguished due to their high echogenicity (i.e., brightness) at the surface. The minimization of acoustic reflections with a rough (2) as compared to smooth (1) PDMS surface is highlighted; the smooth surface appears much brighter than the rough surface.

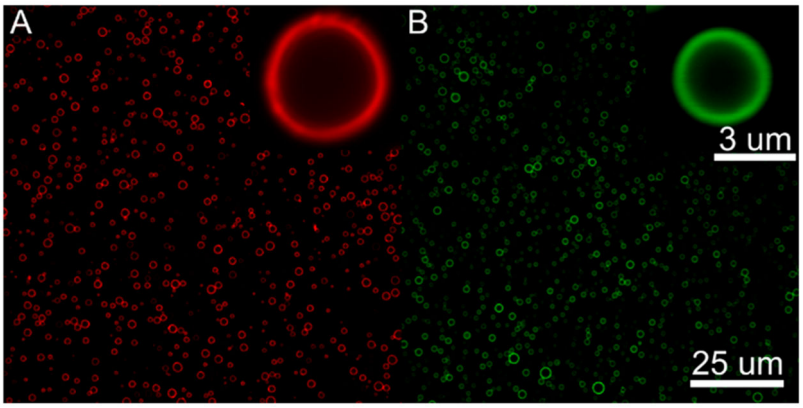

Figure 3.

Confocal microscopy of DiI (A) and Alexa Fluor 488 (B) labeled droplets. The fluorophores and by extension the two lipid populations, DSPC (A) and DSPE-PEG2000 (B), evenly coat the droplet shell. Images and zoomed inserts were captured at 60 X and 1200 X magnification, respectively.

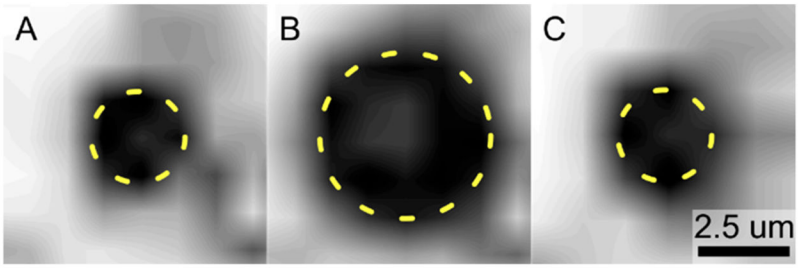

Figure 4.

Acoustic droplet vaporization and recondensation. Images were captured at 580000 frames per second. A single ADV/RC event is shown at $t = 0$ μs (A), $t = 3.44$ μs (B), and $t = 6.88$ μs (C). The droplet (parts A and C) and bubble (part B) diameters are outlined in dashed yellow to highlight the reversible phase change.

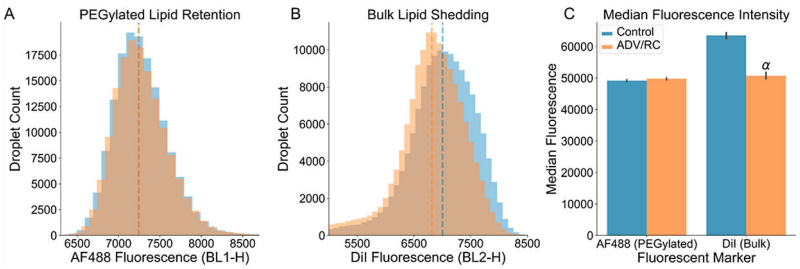

Figure 5.

Flow cytometry results indicating loss of bulk lipids and retention of PEGylated lipids. (A) AF488 fluorescence intensity was used as an analog for relative shell concentration of PEGylated lipids. There was no significant difference between ADV/RC and control groups ($N = 5$, $p > 0.05$), indicating that the PEGylated lipids were fully retained. (B) DiI fluorescence intensity was used as an analog for relative shell concentration of bulk lipids (DSPC). The median fluorescence intensity was significantly lower in the ADV/RC group as compared to controls ($N = 5$, $p < 0.05$). These results indicated that 20% of the bulk lipids were shed during ADV/RC. For both parts A and B, two representative example histograms, illustrating the distribution of droplet fluorescence intensities, are plotted alongside the associated median fluorescence intensity values (dashed vertical lines). (C) Median fluorescence intensity values are plotted, averaged for each group ($N = 5$). Note that values should not be directly compared between AF488 and DiI, as these were two independent droplet populations which used distinct sets of emission filters. PEGylated lipids were retained whereas 20% of the bulk lipids were shed during ADV/RC. α: $p < 0.05$.

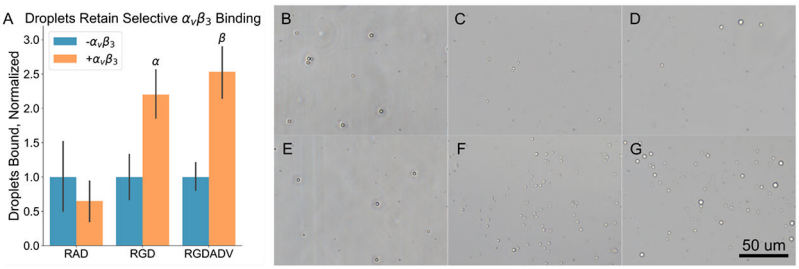

Figure 6.

Droplets retain selective binding capabilities following vaporization and recondensation. (A) A plot of the number of droplets bound within and outside of the $\alpha_v\beta_3$ coated region, normalized to the number bound outside of the $\alpha_v\beta_3$ coated region, is shown. No significant differences were observed in the RAD negative control group, indicating that any enhancement of binding efficacy in the two RGD groups was due to specific receptor–ligand interactions. Both control and ADV/RC RGD groups exhibited significantly more droplets bound within the $\alpha_v\beta_3$ coated region, indicating both groups selectively bound $\alpha_v\beta_3$. α: $p < 0.05$, RGD + $\alpha_v\beta_3$ vs – $\alpha_v\beta_3$. β: $p < 0.05$, RGDADV + $\alpha_v\beta_3$ vs – $\alpha_v\beta_3$. Representative images of RAD, RGD, and RGDADV groups are shown in the – $\alpha_v\beta_3$ (B–D) and + $\alpha_v\beta_3$ (E–F) regions. RGDADV = RGD droplets that underwent ADV/RC.